Linear and nonlinear thermoelectric transport in a magnetic topological insulator nanoribbon with a domain wall

Ning-Xuan Yang [1,2] Qing Yan [1] and Qing-Feng Sun[1,3,4,*]

[1]*International Center for Quantum Materials, School of Physics, Peking University, Beijing 100871, China*

[2]*Department of Physics, College of Sciences, Shihezi University, Shihezi 832000, China*

[3]*Beijing Academy of Quantum Information Sciences, West Bld.3, No.10 Xibeiwang East Rd., Haidian District, Beijing 100193, China*

[4]*Collaborative Innovation Center of Quantum Matter, Beijing 100871, China*

(Received 11 August 2020; accepted 16 November 2020; published 10 December 2020)

We theoretically investigate the thermoelectric transport in the nanoribbon of the magnetic topological insulator with a domain wall in the linear and nonlinear regimes. The Lorenz number L, the Seebeck coefficients S_c, and the thermoelectrical figure of merit ZT in the linear response regime are obtained by the nonequilibrium Green's function method. These thermoelectric coefficients strongly depend on the configuration of the domain wall, that is, the configuration of the domain wall can regulate the thermoelectric transport performance. We also discuss the effect of the width of nanoribbon and the thickness of the domain wall on the thermoelectric coefficient. The results show that the Néel-type wall is more dependent on the size effect of the domain wall than the Bloch-type wall. For a device with a given width, we can always allow the setup to be in high performance thermoelectric transport by adjusting the configuration of the domain wall. Moreover, considering the disorder, the transmission coefficient is robust against disorder even if the disorder strength is very strong, and S_c and ZT are robust against moderate disorder. Finally, for a nonlinear situation, we calculate the maximum power-generation efficiency η and the equivalent thermoelectric figure of merit ZT_M, indicating the potential application as an effective thermoelectric device.

DOI: 10.1103/PhysRevB.102.245412

I. INTRODUCTION

Thermoelectricity is both an ancient and young subject. The thermoelectric effect is the phenomenon of a direct conversion from the heat energy to the electric energy when the temperature gradient exists [1,2]. Since Loffe found a significant thermoelectricity in the doped semiconductors [3–5], huge interests have arisen in thermoelectric phenomena [6–15]. As a clean energy technology, thermoelectric energy conversion technology converts the waste heat produced into the exploitable electric energy, not only alleviating the energy shortage, but also reducing environmental pollution [16,17]. So far, thermoelectric devices are mainly used in situations where reliability and quiet operations are more important than cost, such as the manufacture of portable thermoelectric cooling devices, equipments in medical applications, automotive waste heat automatic recovery devices, space probes, and so on [5,18].

To further promote the application of thermoelectric devices needs to improve the thermoelectric conversion efficiency, denoted by the thermoelectric figure of merit ZT. ZT is defined as $ZT = \sigma {S_c}^2 \mathcal{T}/(\kappa_{\rm el} + \kappa_{\rm ph})$, where σ is the electric conductivity, S_c is the Seebeck coefficient, $\mathcal{T}$ is the absolute temperature of the device, and $\kappa_{\rm el}(\kappa_{\rm ph})$ is the electronic (phononic) contribution to the thermal conductance [2,19–23]. To obtain a large ZT, we must increase the electric conductance σ and the Seebeck coefficient S_c, but simultaneously reduce the thermal conductivity $\kappa = \kappa_{\rm el} + \kappa_{\rm ph}$, that is, the synergistic optimization of electrical and thermal transport properties. Unfortunately, the Mott relation states that the increasing electric conductance σ is usually accompanied with the decreasing of the Seebeck coefficient in normal bulk materials [24,25]. The Wiedemann-Franz law requires that electric conductance σ, the thermal conductivity κ, and temperature satisfy $L \equiv \kappa/\sigma\mathcal{T} = (k_B\pi)^2/3e^2$ with L the Lorentz number and k_B the Boltzmann constant [26–29], which means that a decrease in the thermal conductivity also leads to a decrease in the electric conductivity. As a result, the thermoelectric conversion efficiency is usually limited to $ZT \sim 1$, less than the industrially competitive value $ZT > 3$ [3]. Therefore, it is expected to find sufficiently effective thermoelectric materials with a high ZT to achieve cost-effectiveness [7].

The ZT in nanomaterials has been greatly improved since the limitation by scale and multiple interfaces reduce the thermal conductivity [4,30]. After Hicks and Dresselhaus [31] proposed to use low-dimensional materials to obtain the high ZT, more and more research groups began to focus on thermoelectric transport in nanomaterials. In 1996, the theoretical research of Mahan and Sofo [32] showed that the limitation of the Wiedemann-Franz law can be broken in low-dimensional materials to enhance thermoelectric conversion efficiency. In 2004, Majumdar [3] pointed out that the material scale for improving the thermoelectric conversion efficiency must be at the micronanometer scale. In 2011, Shakouri [33] reviewed advances in semiconductor thermoelectric physics and materials, which provided useful insights for further research on the thermoelectric transport of nanoscale systems.

*sunqf@pku.edu.cn

In recent years, the discovery of topological insulators provided a new research platform for the field of thermoelectric transport. Topological insulators are characterized by the insulating bulk state and the nontrivial conducting edge state or surface state [34–36]. In general, thermoelectric materials should have a high electric conductance and Seebeck coefficient and a low electric thermal conductance to achieve a high ZT value. Narrow bands accomplish high conductance. The heavy elements (with large atomic masses) accomplish low thermal conductance. The construction of topological insulators requires strong spin-orbit coupling, that is, increasing atomic mass is beneficial for the topological phase. Topological insulators need the band inversion, as a result, it usually is a narrow band also. So many topological insulators are also good thermoelectric materials. Although there is no direct relationship, topological insulators have similar material properties as thermoelectric materials, such as heavy elements, narrow band gaps, and the quantum localization effect. Actually, typical three-dimensional (3D) topological insulators (like Bi_2Te_3, Sb_2Te_3, Bi_2Se_3, and Bi_xSb_{1-x}) are considered as promising candidates for materials of thermoelectric conversion [2,19,20,37,38]. In addition, topological insulators have their unique properties, that is, it has the insulating bulk gap and exotic metallic edge states [34–36], which also provides a new way to regulate the electric and thermal conductances. Very recently, Cheng *et al.* [39] found that Cr-doped PbSe has a topological phase transition from the initial banded insulator to the topological crystal insulator where the thermoelectric value ZT is the best. This study provides a new idea for optimizing the performance of thermoelectric materials.

The magnetic topological insulators (MTIs) can be realized by the magnetic doping or the magnetic proximity effect [40–44]. Novel transport phenomena occur in the MTIs, such as the quantum anomalous Hall effect (QAHE), the topological magnetoelectric effect, and the topology axionic polarization exciton [41,43]. As to the experimental progress, in 2013, Chang *et al.* [45] first observed the QAHE in Cr-doped $(Bi, Sb)_2Te_3$ films, which is promising to develop the low consumption electronic devices. In 2014, Wang's group [46] investigated the QAHE and related chiral transport in the millimeter-size Cr-doped $(Bi, Sb)_2Te_3$ films, and for the first time confirmed the scale invariance of dissipative chiral edge states by nonlocal transport measurements. In 2017, two groups [47,48] realized the domain walls of the MTIs in Cr-doped $(Bi, Sb)_2Te_3$ with the tip of a magnetic force microscope. Recently, QAHE was also realized in the intrinsic MTIs $MnBi_2Te_4$ with an innate magnetic order [49].

The domain walls of MTIs are the boundary of two magnetic domains with opposite magnetization directions, see Fig. 1. For magnetic materials, the total magnetic energy is composed of the exchange interaction, the magnetic anisotropy, and the dipole interactions. To minimize the total magnetic energy, the magnetization vector at the domain boundary tends to undergo a continuous change rather than a sharp change, that is, to form a domain wall. The optimized configuration and thickness of the domain wall are determined by the energy competition [50–53]. There are two energetically favorable configurations of domain walls, named after Néel type and Bloch type. The transition between various configurations of the domain wall can be adjusted

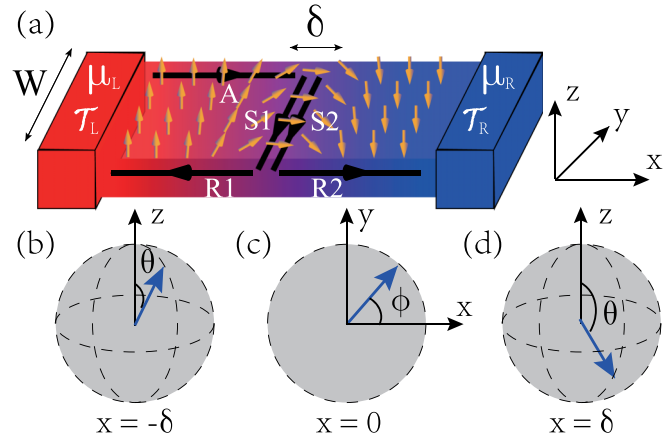

FIG. 1. (a) The schematic cubic diagram of a system. The system consists of a rectangular center MTI nanoribbon with a domain wall at $x = 0$ connected to a hot lead and a cold lead. The black lines with arrows represent the transport processes based on chiral edge modes and interfacial states. A thermal gradient $\Delta\mathcal{T}$ is applied in the x direction. We consider $\Delta\mathcal{T} = \mathcal{T}_L - \mathcal{T}_R > 0$ and $\Delta\mu = \mu_L - \mu_R$ and set $\mathcal{T} = \mathcal{T}_R$. (b)–(d) show the orientation of magnetic moment $\mathbf{M}(x)$ at $x = -\delta$, $x = 0$ and $x = \delta$, respectively. Here θ and ϕ are the polar and azimuthal angles of $\mathbf{M}$. $\phi = 0$ corresponds to the Néel-type domain wall and $\phi = \pi/2$ is a Bloch-type domain wall.

by Dzyaloshinskii-Moriya interaction [50,51,54]. In addition, one of the most important properties of the domain walls of MTIs is the existence of chiral edge states on both sides of the domain wall [52]. The transport through the MTI domain wall strongly depends on the configuration of the domain wall [52]. So we expect that the thermoelectric properties can be regulated by changing the configuration of the domain wall and expect to find the high ZT.

In this paper, we carry out a theoretical study of the thermoelectric transport properties of a MTI nanoribbon with a domain wall. Using the nonequilibrium Green's function method, we find the linear thermoelectric properties strongly depends on the configuration of the domain wall, labeled by the azimuth angle ϕ. The results show the thermoelectrical figure of merit ZT is not maximum for $\phi = 0$ (the Néel type) or $\phi = \pi/2$ (the Bloch type), and ZT can be well controlled by tuning the azimuth angle ϕ. When the temperature varies, the peak value of ZT first increases and then decreases, leading to the maximum when the temperature is at a few tens of Kelvins. In addition, we study how other parameters influence the thermoelectric transport coefficient, including the width of the nanoribbon, the thickness of the domain wall, and the disorder around the domain wall. Results show that the Lorenz number L, the Seebeck coefficient S_c, and ZT are tunable through the width of the nanoribbon and the thickness of the domain wall. Furthermore, S_c and ZT are robust against moderate disorder. Finally, we investigate the thermoelectric effect in the nonlinear regime with a finite bias and temperature gradient. In the nonlinear case, the equivalent thermoelectric figure of merit can be maintained or even increased compared with the linear case, and the thermoelectric efficiency can reach 20% with the temperature gradient at a few tens of Kelvins.

The rest of the paper is organized as follows. In Sec. II, the model and the effective tight-binding Hamiltonian are introduced. The formalisms for calculating thermoelectric parameters are then derived. In Secs. III and IV, we study the thermoelectric properties in the linear regime and the nonlinear regime. Finally, a brief summary is drawn in Sec. V.

II. MODEL AND METHODS

A. Model and Hamiltonian

We consider a two-terminal nanoribbon composed of the MTI with a domain wall at $x = 0$, shown in Fig. 1(a). The y direction is homogeneous and the x direction is the transport direction with the continuous varying magnetic moment labeled by $\mathbf{M}(x)$ [52,53]

$$\begin{aligned}\mathbf{M}(x) &= [M_x(x), M_y(x), M_z(x)] \\ &= M(\sin\theta\cos\phi, \sin\theta\sin\phi, \cos\theta),\end{aligned} \tag{1}$$

where M is the magnitude of the magnetization, (θ, ϕ) are the polar angle and the azimuth angle in the spherical coordinate system, labeling the orientation of the magnetic moment $\mathbf{M}(x)$. Here, ϕ is independent of the coordinate x, but θ is a function of x with $\cos\theta(x) = -\tanh\frac{x}{\delta}$ where δ denotes the thickness of the domain wall. The magnetic moment $\mathbf{M}(x)$ aligns in the $+z$ direction when $x \ll 0$ and in the $-z$ direction when $x \gg 0$, but $\mathbf{M}(x)$ continuously changes from upward to downward from $x < 0$ through $x = 0$ to $x > 0$. Figs. 1(b), 1(c), and 1(d) show the orientation of $\mathbf{M}(x)$ at $x = -\delta$, $x = 0$ and $x = \delta$, respectively. At $x = 0$, the magnetic moment $\mathbf{M}(x)$ is in the x-y plane as shown in Fig. 1(c). The way that $\mathbf{M}(x)$ varies is regarded as the configuration of the domain wall, labeled by the azimuth angle ϕ: $\phi = 0$ and $\phi = \pi/2$ correspond to the Néel-type wall and the Bloch-type wall, respectively [52].

Considering the low-energy state, the nanoribbon of the MTI with a domain wall can be described in with a continuous Hamiltonian as follows [43,52,53,55,56]:

$$H = \sum_{\mathbf{p}} c_{\mathbf{p}}^{\dagger}[v_F(p_y\tau_z\sigma_x - p_x\tau_z\sigma_y) + m(\mathbf{p})\tau_x + \mathbf{M}(x)\cdot\sigma]c_{\mathbf{p}}, \tag{2}$$

where $\mathbf{p} = (p_x, p_y)$ and $c_{\mathbf{p}} = [c_{\mathbf{p}t\uparrow}, c_{\mathbf{p}t\downarrow}, c_{\mathbf{p}b\uparrow}, c_{\mathbf{p}b\downarrow}]^T$ is a four-component electron operator. Here, t and b label electrons in the top and bottom layers and $\uparrow$ and $\downarrow$ denote electrons with up and down spins. Moreover, $\sigma = (\sigma_x, \sigma_y, \sigma_z)$ and (τ_x, τ_y, τ_z) are Pauli matrices for the spin and layer spaces, respectively. $m(\mathbf{p}) = m_0 - m_1(p_x^2 + p_y^2)$ describes the coupling between the top and bottom layers [52].

Based on the Hamiltonian in Eq. (2), we can discrete the continuous model into a lattice version [52,53,57–59]

$$\begin{aligned}H &= \sum_{\mathbf{j}}[c_{\mathbf{j}}^{\dagger}R_0c_{\mathbf{j}} + c_{\mathbf{j}}^{\dagger}R_xc_{\mathbf{j}+\delta x} + c_{\mathbf{j}}^{\dagger}R_yc_{\mathbf{j}+\delta y} + \text{H.c.}], \\ R_0 &= \left(m_0 - \frac{4m_1}{a^2}\right)\tau_x + \mathrm{M}\cdot\sigma, \quad R_x = \frac{m_1}{a^2}\tau_x + \frac{iv_F}{2a}\tau_z\sigma_y, \\ R_y &= \frac{m_1}{a^2}\tau_x - \frac{iv_F}{2a}\tau_z\sigma_x,\end{aligned} \tag{3}$$

where $c_{\mathbf{j}} = [c_{\mathbf{j}t\uparrow}, c_{\mathbf{j}t\downarrow}, c_{\mathbf{j}b\uparrow}, c_{\mathbf{j}b\downarrow}]^T$ is the annihilation operator at site $\mathbf{j} = (x, y)$. In the calculation, we set the lattice constant $a = 0.6$ nm, the Fermi velocity $v_F = 0.222$ eVnm, the parabolic term $m_0 = 0.026$ eV and $m_1 = 0.137\,\text{eVnm}^2$, and the magnitude of magnetization $M = 0.048$ eV [52,60].

B. Linear response regime

In the linear response regime, the electric current I_C and the heat current I_Q are expanded to the linear order in $\Delta\mathcal{T} = \mathcal{T}_L - \mathcal{T}_R$ and $\Delta V = V_L - V_R$ [21,61,62],

$$\begin{pmatrix} I_C \\ I_Q \end{pmatrix} = \begin{pmatrix} e^2L_0 & -eL_1 \\ -eL_1 & L_2 \end{pmatrix}\begin{pmatrix} \Delta V \\ \Delta\mathcal{T}/\mathcal{T} \end{pmatrix}. \tag{4}$$

The elements of the Onsager matrix in Eq. (4) are fully determined by the transmission coefficient $T(E)$ as follows:

$$L_i = \frac{1}{h}\int dE(E - E_F)^i\left(-\frac{\partial f}{\partial E}\right)T(E), \quad i = 0, 1, 2, \tag{5}$$

where $f(E) = [e^{(E-E_F)/k_B\mathcal{T}} + 1]^{-1}$ is the Fermi distribution function. We obtain the transmission coefficient $T(E)$ using the nonequilibrium Green's function method [63],

$$T(E) = \mathrm{Tr}[\mathbf{\Gamma}_{\mathrm{L}}\mathbf{G}^r\mathbf{\Gamma}_{\mathrm{R}}\mathbf{G}^a], \tag{6}$$

where $\mathbf{\Gamma}_{\mathrm{L/R}}(E) = i[\mathbf{\Sigma}^r_{\mathrm{L/R}}(E) - \mathbf{\Sigma}^a_{\mathrm{L/R}}(E)]$ and the Green's function $\mathbf{G}^r(E) = [\mathbf{G}^a]^{\dagger} = [E\mathbf{I} - \mathbf{H}_{\mathrm{cen}} - \sum_{\alpha}\mathbf{\Sigma}^r_{\alpha}]^{-1}$ with $\mathbf{H}_{\mathrm{cen}}$ being the Hamiltonian of the center scattering region and the self-energy $\mathbf{\Sigma}^{r/a}_{\mathrm{L/R}}$ stemming from the coupling with the left/right lead [62–64].

The linear electric conductance G, the Seebeck coefficients S_c, and the electric thermal conductance κ_{el} are obtained from Eq. (4) [21,61,62]

$$G = \lim_{\Delta V\to 0}\frac{I_C}{\Delta V}\Big|_{\Delta\mathcal{T}=0} = e^2L_0(\mathcal{T}), \tag{7}$$

$$S_c = -\lim_{\Delta\mathcal{T}\to 0}\frac{\Delta V}{\Delta\mathcal{T}}\Big|_{I_C=0} = -\frac{1}{e\mathcal{T}}\frac{L_1(\mathcal{T})}{L_0(\mathcal{T})}, \tag{8}$$

$$\kappa_{\mathrm{el}} = -\lim_{\Delta\mathcal{T}\to 0}\frac{I_Q}{\Delta\mathcal{T}}\Big|_{I_C=0} = \frac{1}{\mathcal{T}}\left[L_2(\mathcal{T}) - \frac{L_1^2(\mathcal{T})}{L_0(\mathcal{T})}\right]. \tag{9}$$

The ratio between the electric thermal conductance κ_{el} and the electric conductance G denotes the Lorenz number L [65],

$$L = \frac{\kappa_{\mathrm{el}}}{G\mathcal{T}} = \frac{1}{e^2\mathcal{T}^2}\cdot\frac{L_0L_2 - L_1^2}{L_0^2}. \tag{10}$$

In addition, the thermoelectric figure of merit ZT is used as a dimensionless parameter in the literature of heat transport. Neglecting the lattice thermal conductance κ_{ph} due to $\kappa_{\mathrm{ph}} \ll \kappa_{\mathrm{el}}$ at the low temperature, ZT can be obtained straightforwardly, $ZT = GS_c{}^2\mathcal{T}/\kappa_{\mathrm{el}} = S_c{}^2/L = \frac{L_1^2}{L_0L_2 - L_1^2}$.

In addition, the local transport current from sites $\mathbf{i}$ to $\mathbf{j}$ for the incident electron from the left MTI lead with the energy E is [59,66–68]

$$J_{\mathbf{ij}} = -\frac{2e^2}{h}\mathbf{Im}\mathrm{Tr}\big[H_{\mathbf{ij}}\mathbf{G}^L_{\mathbf{ji}}(E)\big], \tag{11}$$

with $\mathbf{G}^L(E) = \mathbf{G}^r(E)\mathbf{\Gamma}_L(E)\mathbf{G}^a(E)$. The local occupation number at the site $\mathbf{j}$ is given by $N_{\mathbf{j}} = \langle c_{\mathbf{j}}^{\dagger}c_{\mathbf{j}}\rangle = -i\int \mathrm{Tr}\,\mathbf{G}^<_{\mathbf{jj}}(E)dE = \int \mathrm{Tr}\{[\mathbf{G}^r(\mathbf{\Gamma}_{\mathrm{L}}f_{\mathrm{L}} + \mathbf{\Gamma}_{\mathrm{R}}f_{\mathrm{R}})\mathbf{G}^a]_{\mathbf{jj}}\}dE = \int n_{\mathbf{j}}(E)dE$,

where we applied the Keldysh equation $\mathbf{G}^<(E) = \mathbf{G}^r(E)[i\mathbf{\Gamma}_L f_L + i\mathbf{\Gamma}_R f_R]\mathbf{G}^a(E)$ [66,69]. Then we get the expression of the local occupation number $n_{\mathbf{j}}^L(E)$ for incident electron from the left MTI lead with the energy E:

$$n_{\mathbf{j}}^L(E) = \mathrm{Tr}\{[\mathbf{G}^r(E)\Gamma_L(E)\mathbf{G}^a(E)]_{\mathbf{jj}}\} = \mathrm{Tr}\{\mathbf{G}_{\mathbf{jj}}^L(E)\}. \quad (12)$$

C. Nonlinear regime

In the nonlinear regime, the temperature gradient $\Delta\mathcal{T}$ and bias ΔV are finite, with $\Delta\mathcal{T} = \mathcal{T}_L - \mathcal{T}_R$ and $\Delta V = (\mu_L - \mu_R)/e$. Here the temperature gradient $\Delta\mathcal{T}$ is set larger than 0. The electric current from the left lead to the right lead is given by the expression [7–9,65]

$$I_C = \frac{e}{h}\int dE T(E)[f_L(\mu_L, \mathcal{T}_L; E) - f_R(\mu_R, \mathcal{T}_R; E)], \quad (13)$$

where $f_\alpha(\mu_\alpha, \mathcal{T}_\alpha; E) = [e^{(E-\mu_\alpha)/k_B\mathcal{T}_\alpha} + 1]^{-1}$ is the Fermi function of the α lead with the chemical potential μ_α at temperature $\mathcal{T}_\alpha$ ($\alpha = L, R$). The expression for the heat current in the α lead can be derived by the first law of thermodynamics

$$I_\alpha^Q = \frac{1}{h}\int dE(E-\mu_\alpha)T(E)[f_L(\mu_L, \mathcal{T}_L; E) - f_R(\mu_R, \mathcal{T}_R; E)]. \quad (14)$$

Hereafter, we regard this device as a power generator with the power output P,

$$P = -I_C\Delta V = \frac{1}{h}(\mu_R - \mu_L)\int dE T(E)[f_L(\mu_L, \mathcal{T}_L; E) - f_R(\mu_R, \mathcal{T}_R; E)]. \quad (15)$$

We set μ_R to be higher than μ_L satisfying $P > 0$ in the heat engine. The efficiency of the power generator is given by the generated electric power divided by the heat lost from the hot lead [7–9,65]

$$\eta = \frac{P}{I_L^Q} = \frac{(\mu_R - \mu_L)\int dE T(E)[f_L(\mu_L, \mathcal{T}_L; E) - f_R(\mu_R, \mathcal{T}_R; E)}{\int dE(E-\mu_L)T(E)[f_L(\mu_L, \mathcal{T}_L; E) - f_R(\mu_R, \mathcal{T}_R; E)]}. \quad (16)$$

In the calculation, we fix the temperatures $\mathcal{T}_{L/R}$ and the chemical potential μ_L, and change μ_R, so that the power-generation efficiency η reaches the maximum value. Then considering that the maximum power-generation efficiency of a thermoelectric device is related to the dimensionless figure of merit [2],

$$\eta = \frac{\mathcal{T}_L - \mathcal{T}_R}{\mathcal{T}_L}\cdot\frac{\sqrt{1+ZT_M}-1}{\sqrt{1+ZT_M}+\frac{\mathcal{T}_R}{\mathcal{T}_L}}, \quad (17)$$

the equivalent thermoelectric figure of merit is derived in terms of η,

$$ZT_M = \left[\frac{(\mathcal{T}_L - \mathcal{T}_R) + \eta\mathcal{T}_R}{(\mathcal{T}_L - \mathcal{T}_R) - \eta\mathcal{T}_L}\right]^2 - 1. \quad (18)$$

We set the temperature of the right lead to be the same as the background temperature $\mathcal{T}_R = \mathcal{T}$ and the temperature of the left lead to be $\mathcal{T}_L = \mathcal{T} + \Delta\mathcal{T}$. Thus, Eqs. (17) and (18) lead to the maximum power-generation efficiency $\eta = \frac{\Delta\mathcal{T}}{\mathcal{T}+\Delta\mathcal{T}}\frac{\sqrt{1+ZT_M}-1}{\sqrt{1+ZT_M}+\mathcal{T}/(\mathcal{T}+\Delta\mathcal{T})}$ and the equivalent figure of merit $ZT_M = [\frac{\Delta\mathcal{T}+\eta\mathcal{T}}{\Delta\mathcal{T}-\eta(\mathcal{T}+\Delta\mathcal{T})}]^2 - 1$.

III. THERMOELECTRIC PROPERTIES IN LINEAR RESPONSE

In this section, we study the thermoelectric transport property of the MTIs nanoribbon in the linear regime, i.e., the temperature gradient $\Delta\mathcal{T} \to 0$. In the numerical calculation, we set the width of the nanoribbon as $W = 90$ nm and the thickness of the domain wall as $\delta = 1.5$ nm throughout this paper unless otherwise mentioned, and then focus on how the configuration of the domain wall labeled by the azimuth angle ϕ affects the transport. Figure 2 shows the transmission coefficient T as a function of the incident energy E with different configurations of domain walls. Here, the azimuthal angle picks values of $\phi = 0, \pi/12, \pi/6, \pi/4, \pi/3, 5\pi/12$, and $\pi/2$.

It can be seen from the figure that when the incident energy E is high in the conduction band or the valence band of the left/right MTIs (i.e., $E \geqslant 0.025$ eV or $E \leqslant -0.025$ eV with the bulk gap Δ_b of the MTIs being about 0.025 eV) [52], the transmission coefficients for all azimuth angles ϕ are relatively large, but the difference between them is small. For the incident energy within the bulk gap, $-\Delta_b \leqslant E \leqslant \Delta_b$, the chiral edge states dominate the transport processes, the transmission coefficients are less than 1 regardless of ϕ because there is only one incident edge mode in the left MTIs

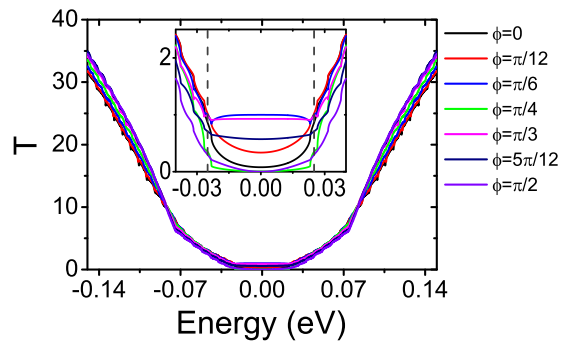

FIG. 2. The transmission coefficient T of the device in Fig. 1 as a function of incident energy E for several ϕ with width of system $W = 90$ nm, in which the x-axis is the transport direction. The insets in panels are the zoomed-in figures of the mixed curves in the corresponding main figure. The vertical dotted lines show the bulk gap Δ_b and $-\Delta_b$.

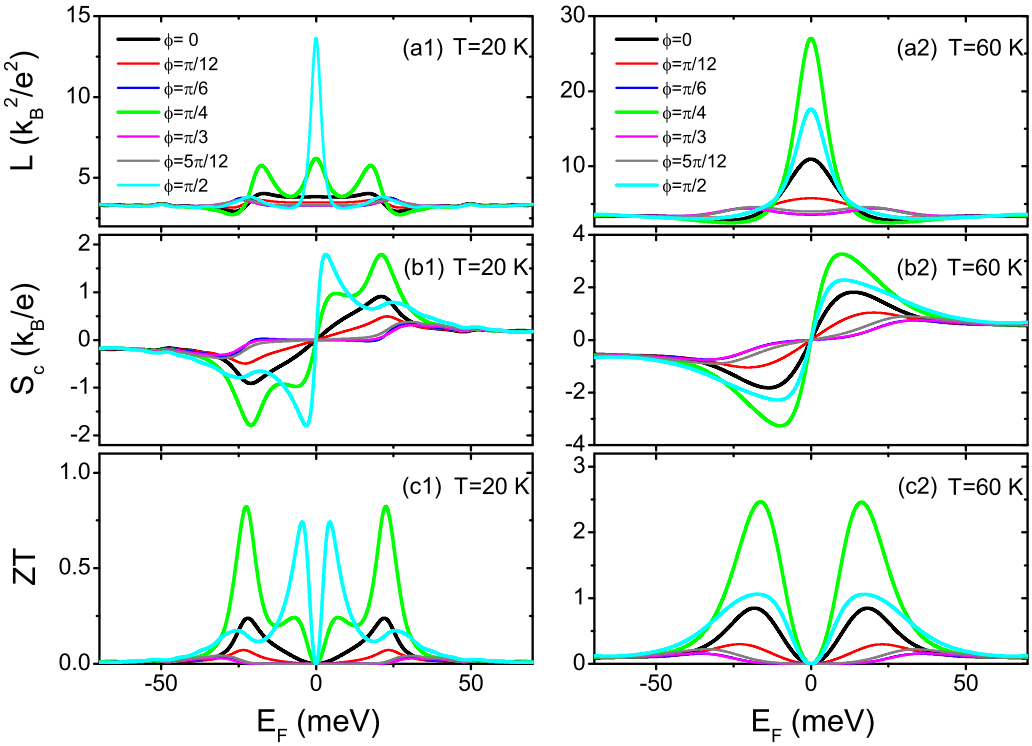

FIG. 3. The Lorenz number L, the Seebeck coefficients S_c, and the thermoelectric figure of merit ZT as functions of Fermi energy E_F for several ϕ with temperature $\mathcal{T} = 20$ K in (a1), (b1), (c1) and $\mathcal{T} = 60$ K in (a2), (b2), (c2). The width of system W is 90 nm and the domain wall thickness δ is 1.5 nm.

lead, see Fig. 1(a). In addition, in the low-energy case, the transport behavior of chiral edge states at the domain wall of MTIs strongly depends on the configuration of domain walls [52], so we can see that transmission coefficients show a huge difference among different configurations of the domain wall [see the zoom-in figure of Fig. 2]. When the incident electron energy is close to 0, the transmission coefficients with $\phi = \pi/4$ and $\pi/2$ are very small, approximately in the order of 10^{-3}, which is much smaller than those with other values of ϕ, so a large quasitransport gap will be formed when $\phi = \pi/4$ and $\pi/2$. Generally speaking, the transport gap can result in a large S_c and ZT [62,70–72] because of the sudden jump of the transmission coefficient in the vicinity of the gap edge, which is very beneficial for thermoelectric transport. In addition, the transmission coefficient $T(E)$ and the transport gap is easily adjusted by varying ϕ, which means that we can also tune S_c and ZT. Moreover, we find that for all the azimuthal angle ϕ, the transmission coefficient T is symmetric about $\phi = \pi/2$, i.e., $T(\phi) = T(\pi - \phi)$.

Figure 3 displays the Lorenz number L, the Seebeck coefficients S_c, and the thermoelectric figure of merit ZT as functions of the Fermi energy E_F. When E_F is deep in the conduction or valence band of the left/right MTIs lead, the bulk states dominate the transport process, the Lorenz number L is almost equal $\frac{(k_B\pi)^2}{3e^2}$, and the Wiedemann-Franz law well holds, resulting in very small Seebeck coefficient and ZT. On the other hand, when E_F locates in the gap, the electron propagates along the chiral edge states, the Wiedemann-Franz law is broken and the Lorenz number L, $|S_C|$, and ZT can be very large. At low temperature (e.g., $\mathcal{T} = 20$ K), thermoelectric coefficients (L, S_c, and ZT) vary in the shape of curves with different peak values for different configurations of domain walls. This indicates that the configurations of domain walls can regulate the thermoelectric transport performance. When $\phi = \pi/4$ and $\pi/2$, the values of L, S_c, and ZT are larger than those of other azimuthal angles ϕ [see Figs. 3(a1), 3(b1), and 3(c1)]. For $\mathcal{T} = 60$ K, L, S_c, and ZT share similar trends but present different peaks values. For the Lorenz number L, the largest peak appears at $E_F = 0$. S_c and ZT have the highest peak near $E_F = 0$. The comparison among Figs. 3(a2), 3(b2), and 3(c2) shows the largest thermoelectric coefficients appear when the azimuthal angle $\phi = \pi/4$ because there is a large transport gap at $\phi = \pi/4$. When E_F crosses the transport gap, the transmission coefficient T abruptly jumps from almost zero to a finite value (see Fig. 2), so S_c and ZT show a large peak.

Next, we focus on how the temperature affects the thermoelectric transport of three specific configurations of domain walls in detail. Figure 4 shows the Lorenz number L, the Seebeck coefficient S_c, and the thermoelectric figure of merit ZT versus Fermi energy E_F at different temperatures. The Lorenz number L is an even function of E_F with $L(-E_F) = L(E_F)$. L shows a large peak near $E_F = 0$ of which the value is depended on the temperature and the azimuth angle. The peak of L with $\phi = \pi/4$ is sharper and higher than that with $\phi = 0$ or $\pi/2$ but the half-high width of $\phi = 0$ or $\pi/2$ is definitely larger than that of $\phi = \pi/4$. Figure 4(a2) shows the largest L at temperature $\mathcal{T} = 60$ K. The temperature also influences S_c and ZT. For $|S_c|$ and ZT, two large peaks appear symmetrically on both sides of the Fermi energy $E_F = 0$. S_c is an odd function of the Fermi energy E_F with $S_c(-E_F) = -S_c(E_F)$.

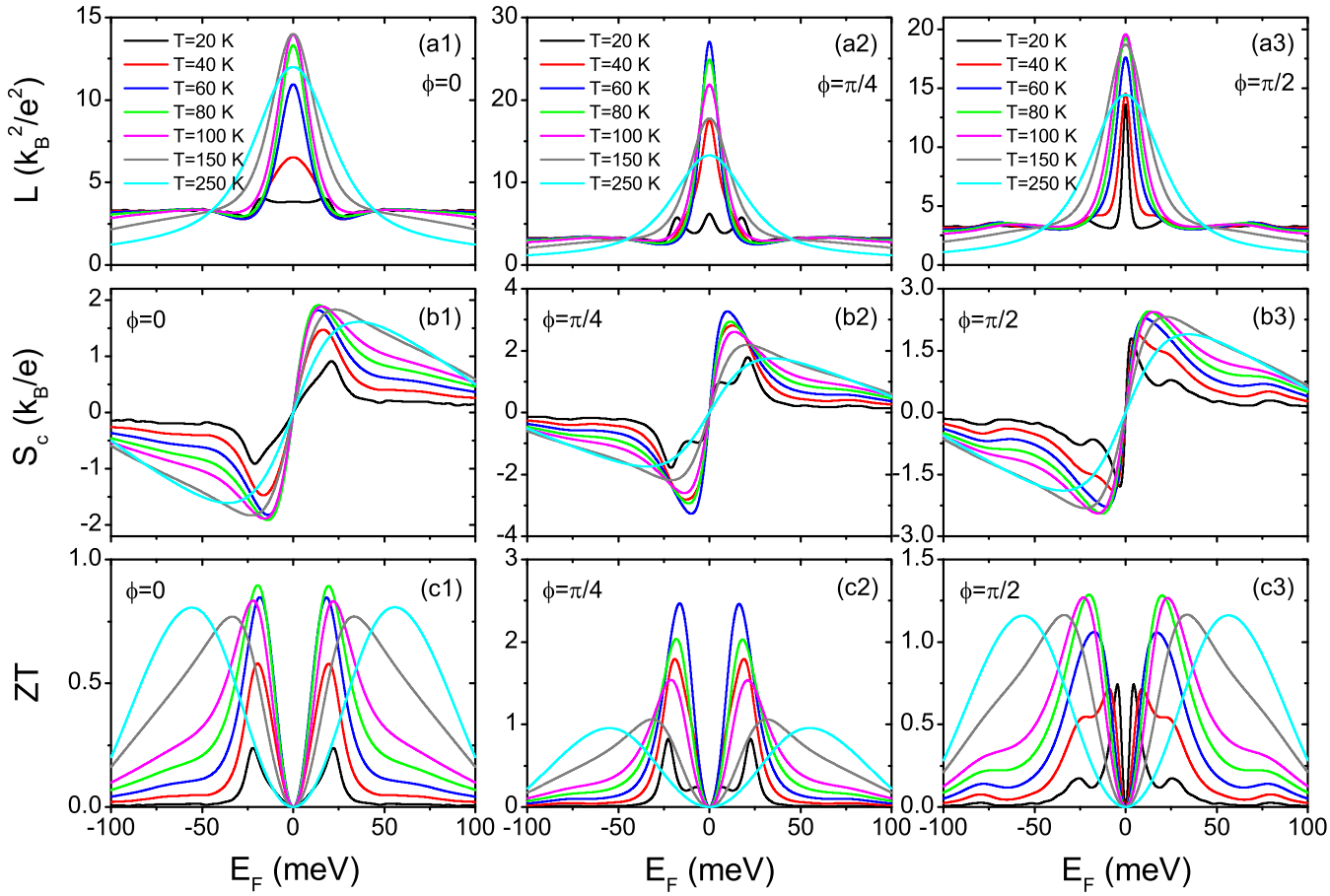

FIG. 4. The Lorenz number L, the Seebeck coefficients S_c, and ZT versus Fermi energy E_F for different temperatures and for the Néel wall ($\phi = 0$) in (a1), (b1), (c1); $\phi = \pi/4$ domain wall in (a2), (b2), (c2); and Bloch wall ($\phi = \pi/2$) in (a3), (b3), (c3). The other unmentioned parameters are the same as in Fig. 2.

ZT is an even function of E_F with $ZT(-E_F) = ZT(E_F)$. For many thermoelectric transport systems, ZT decreases rapidly as the temperature increases and picks a large value only when the temperature is very low (maybe several Kelvins) [15,62,73,74]. But for the present system, with the increase of $\mathcal{T}$, ZT first increases and then decreases, leading to the largest value at $\mathcal{T} = 60$ K, $ZT \approx 3$. Considering that the optimal ZT is obtained about at $\mathcal{T} = 60$ K, the current device is possibly suitable for space probes or in some low temperature environments.

Given that impurities and disorders exist inevitably in real materials, the thermoelectric transport may be affected by the impurity scattering mechanism. So below we study the effect of the disorder on the thermoelectric transport. Based on the MTI nanoribbon described in Sec. II, we introduce the Anderson-type disorder in the central region via adding a term $D_i\sigma_0\tau_0$ to the on-site energy R_0 in Eq. (3). D_i is uniformly distributed in the interval $[-D/2, D/2]$ with the disorder strength D. The disorder of possessive points is random and independent of each other. In the numerical calculation, the width of the disordered region is the same as the width of nanoribbon, and its length is chosen as 48 nm to completely cover the domain wall. With each value of disorder strength D, the transmission coefficient T and thermoelectric coefficients (S_c, ZT) are averaged up to 40 configurations.

Figure 5 shows the Seebeck coefficients S_c and the thermoelectric figure of merit ZT with different disorder strength. For three configurations of domain walls, $\phi = 0, \pi/4$, and $\pi/2$, the additional disorder hardly changes the transmission coefficients even if the disorder strength is much larger than the bulk gap, because of the robustness of the MTIs. Figures 5(a) and 5(b) show that S_c and ZT are robust against disorder also. For S_c, disorder does not affect the changing trend of the curves. With the Néel-type domain wall ($\phi = 0$), S_c is robust against moderate disorder. However, S_c is very robust against strong disorder in $\phi = \pi/4$ domain wall and Bloch-type domain wall ($\phi = \pi/2$). As to ZT, in the Néel-type domain wall and $\phi = \pi/4$ domain wall, with the increase of the disorder strength D, the heights of the peaks of S_c and ZT are gradually reduced. The position of peaks slightly shifts as well. The peak value of ZT maintains its amount in the Bloch-type domain wall for all disorder strength D. The peak with the azimuthal angle $\phi = \pi/4$ preserves its value for disorder of the moderate strength ($D = 0.05$ and 0.01) and slightly reduces at strong disorder ($D = 0.15$) but is still larger than 2. The robustness is crucial for the experiment and further application. In addition, the symmetrical properties, $S_c(-E_F) = -S_c(E_F)$ and $ZT(-E_F) = ZT(E_F)$, are slightly destroyed by the disorder, but $S_c(-E_F)$ $[ZT(-E_F)]$ still approximatively equals $-S_c(E_F)$ $[ZT(E_F)]$.

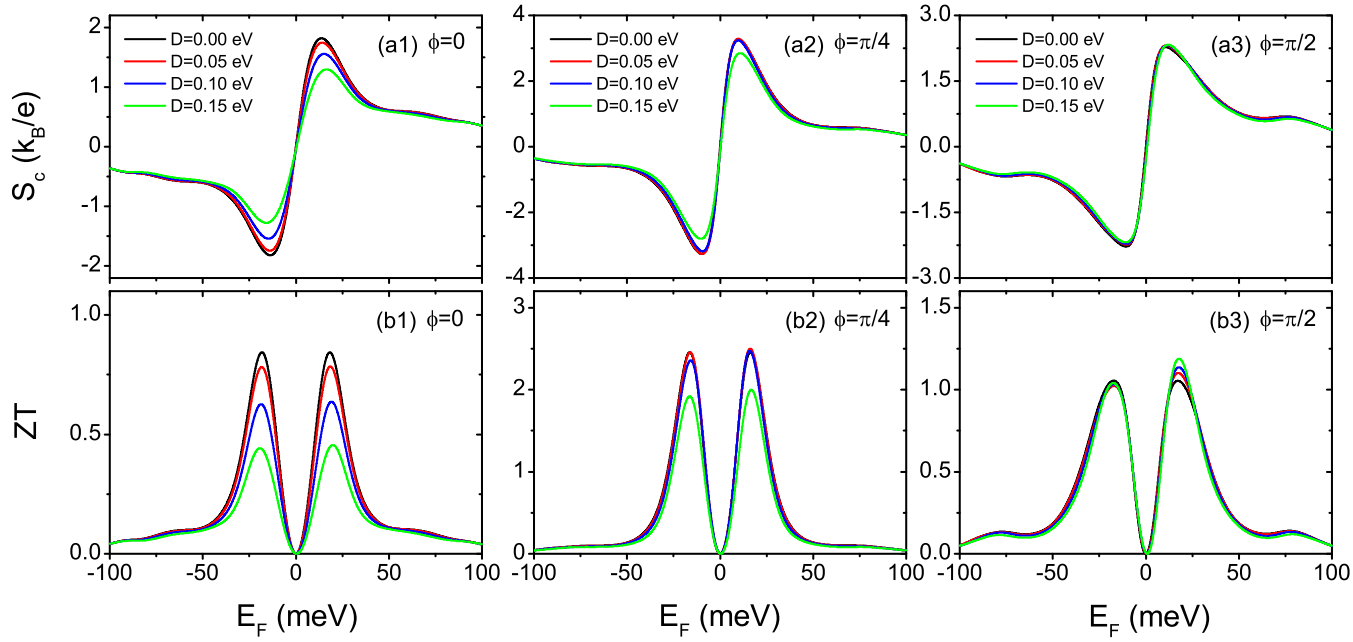

FIG. 5. (a) S_c vs E_F and (b) ZT vs E_F at the different disorder strength D with temperature $\mathcal{T} = 60$ K for Néel wall ($\phi = 0$) in (a1, b1), $\phi = \pi/4$ domain wall in (a2, b2), and Bloch wall ($\phi = \pi/2$) in (a3, b3). The other unmentioned parameters are the same as in Fig. 2.

Let us study how the width of the nanoribbon W and the thickness of the domain wall δ affect the thermoelectric transport. Figures 6(a), 6(b), and 6(c) show thermoelectrical figure of merit ZT as functions of Fermi energy E_F for several widths W with the azimuthal angle $\phi = 0$, $\pi/4$, and $\pi/2$ at temperature $\mathcal{T} = 60$ K. The comparative study to find that L, S_c, and ZT are closely related to the width W. The thermoelectric transport performance of the Néel-type wall is more dependent on the nanoribbon's width W than that of the Bloch-type wall. For the azimuthal angle $\phi = 0$ or $\pi/4$ [see Figs. 6(a) and 6(b)], when $W = 90$ nm, ZT reach their largest values with $\delta = 1.5$ nm. For $\phi = \pi/2$ [see Fig. 6(c)], with the

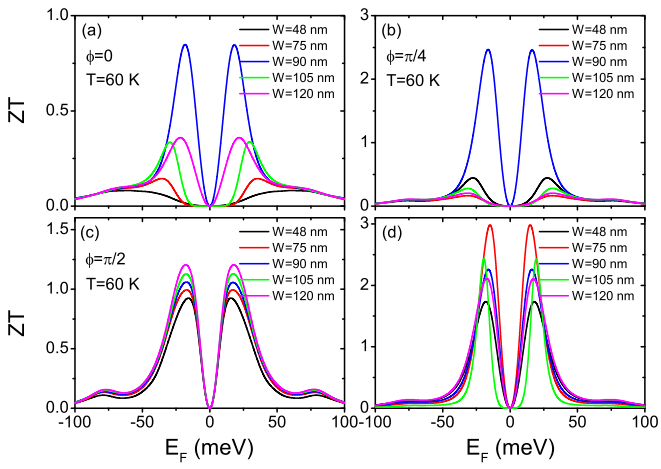

FIG. 6. ZT as functions of Fermi energy E_F for several widths W with temperature $\mathcal{T} = 60$ K, and Néel wall ($\phi = 0$) in (a), $\phi = \pi/4$ domain wall in (b), and Bloch wall ($\phi = \pi/2$) in (c). Panel (d) plots the optimized ZT vs. Fermi energy E_F for several widths W with taking a specific azimuthal angle ϕ and temperature $\mathcal{T}$. The domain wall thickness $\delta = 1.5$ nm.

increase of the width W, ZT slightly increases, and the width $W = 120$ nm, the ZT is maximum.

In fact, for the different width of nanoribbon W, we can optimize the ZT value by changing the azimuthal angle ϕ and temperature $\mathcal{T}$. In the calculation of finding the optimized ZT, for a given width of nanoribbon W, the azimuthal angle ϕ changes from 0, 0.1, 0.2, . . . , 1.4 to $\pi/2$, and the temperature $\mathcal{T}$ takes 20, 25, 30, ..., 120 K. Figure 6(d) shows the optimized ZT as functions of Fermi energy E_F for several widths W with taking a specific azimuthal angle and temperature. For $W = 48$, 75, 90, 105, and 120 nm, the optimized ZT corresponds to the azimuthal angle $\phi = 0.9$, 0.6, 0.8, 0.4, and 1.0 and temperature $\mathcal{T} = 70$, 55, 60, 40, and 65 K, respectively. This means that for a given device width, we can always allow the setup to be in high thermoelectric performance by adjusting the configuration of the domain wall and the background temperature.

Figures 7(a), 7(b), and 7(c) show thermoelectrical figure of merit ZT as functions of Fermi energy E_F for several domain wall thicknesses δ with the azimuth angle $\phi = 0$, $\pi/4$, and $\pi/2$ at temperature $\mathcal{T} = 60$ K. L, S_c, and ZT also strongly depend on the thickness of the domain wall δ. In particular, for the Néel-type wall ($\phi = 0$), the thermoelectrical coefficient is very sensitive to the domain wall thicknesses δ. With fixed $W = 90$ nm, the thermoelectrical figure of merit ZT is the largest at $\delta = 1.5$ nm with the configuration of domain wall $\phi = 0$ or $\pi/4$ [see Figs. 7(a) and 7(b)]. For $\phi = \pi/2$ (the Bloch-type wall) [see Fig. 7(c)], ZT evidently increases with δ decreases. So the ZT is maximum when $\delta = 0.5$ nm.

Figure 7(d) shows the optimized ZT as functions of Fermi energy E_F for several domain wall thicknesses δ with taking a specific azimuthal angle and temperature. For a given thickness of domain wall δ, the azimuthal angle ϕ varies from 0, 0.1, 0.2, . . . , 1.4 to $\pi/2$, and the temperature $\mathcal{T}$ takes 20, 25, 30,. . ., 120 K to find the optimized ZT. Calculated

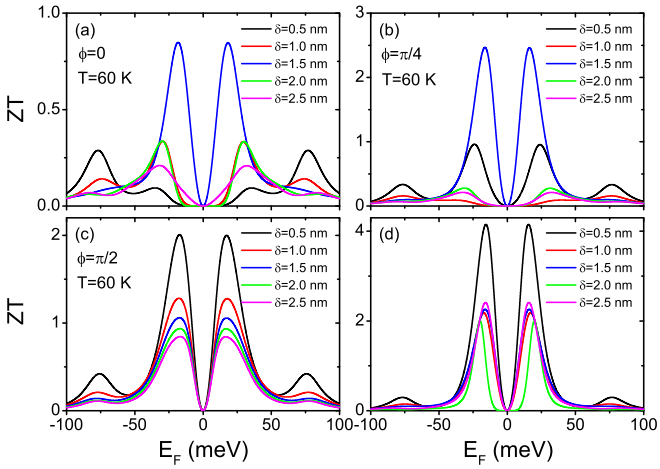

FIG. 7. ZT as functions of Fermi energy E_F for several domain wall thicknesses δ with temperature $\mathcal{T} = 60$ K, and Néel wall ($\phi = 0$) in (a), $\phi = \pi/4$ domain wall in (b), and Bloch wall ($\phi = \pi/2$) in (c). Panel (d) plots the optimized ZT vs. Fermi energy E_F for several domain wall thicknesses δ with taking a specific azimuthal angle ϕ and temperature $\mathcal{T}$. The width of the device $W = 90$ nm.

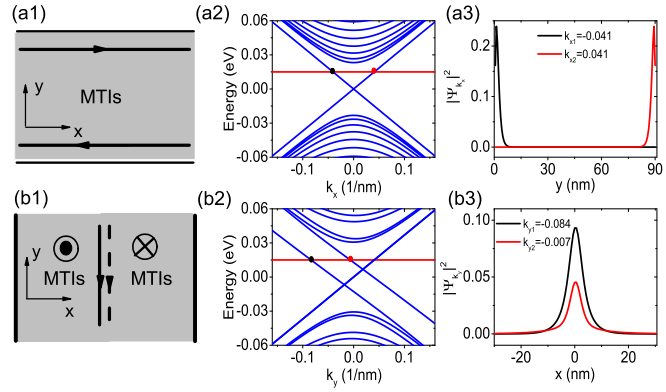

FIG. 8. (a1) The schematic diagram of MTI nanoribbon without the domain wall. Here the nanoribbon is infinite in the x direction with the width W ($W = 90$ nm) in the y direction. The black lines with arrows represent the chiral edge states. (a2) The band structure versus the wave vector k_x. (a3) The wave function $|\Psi_{k_x}|^2$ as a functions of site y for the state marked in (a2) with $E = 0.015$ eV. (b1) The schematic diagram of MTI nanoribbon with a domain wall. Here the nanoribbon is infinite in the y direction with the width L ($L = 60.6$ nm) in the x direction. The azimuthal angle of domain wall $\phi = \pi/4$ and thickness of domain wall $\delta = 1.5$ nm. The black lines with arrows represent the interfacial states along the domain wall. (b2) The band structure versus k_y. (b3) The wave function $|\Psi_{k_y}|^2$ as a functions of site x for the state marked in (b2) with $E = 0.015$ eV. The other unmentioned parameters are the same as in Fig. 2.

results are as follows: when $\delta = 0.5$, 1.0, 1.5, 2.0, and 2.5 nm, the optimized ZT corresponds to the azimuthal angle ϕ=0.7, 0.5, 0.8, 0.4, and 0.6 and the temperature $\mathcal{T} = 55$, 60, 60, 40, and 55 K, respectively. The results show that no matter what the domain wall thickness is, we can get a large ZT by adjusting the configuration of the domain wall (i.e., ϕ). With the decrease of the domain wall thickness, the optimized ZT tends to increase, although it is not monotonically increasing. For the domain wall thickness $\delta = 0.5$ nm, the optimized ZT exceeds 4.

In short, we found that these thermoelectric coefficients (the Lorenz number L, the Seebeck coefficient S_c, and ZT) strongly depend on the configuration of the domain wall ϕ, the thickness of the domain wall δ, and the width of the nanoribbon W. This gives us a way to get a large ZT by tuning the parameters ϕ, δ, and W. In addition, the results also show that the Néel-type wall is more dependent on δ and W than the Bloch-type wall. In the following, we explain these results by using the chiral edge states and the interfacial states.

The MTI has a bulk gap and a pair of gapless chiral edge states. For example, for the parameters of Fig. 2, the gap Δ_b is about 0.025 eV. To show the chiral edge states, we consider a perfect MTI nanoribbon without the domain wall. The nanoribbon is infinite in the x direction with the width W in the y direction, as shown in Fig. 8(a1). Its Hamiltonian is the same as Eq. (2), but the magnetic moment $\mathbf{M}(x) = (0, 0, M)$ is independent of the coordinate x. This nanoribbon is equivalent to the left MTI lead. Figure 8(a2) shows the band structure, which consists of a series of bulk states and two chiral edge states [52]. The chiral edge states are gapless and intersect in the bulk gap. The wave functions $|\Psi_{k_x}|^2$ of the chiral edge states versus the coordinate y for the energy $E = 0.015$ eV (in the bulk gap) are shown in Fig. 8(a3). The wave functions mainly distribute the boundary of the nanoribbon. From the wave functions and band structure in Figs. 8(a2) and 8(a3), we can obtain that the chiral edge state at the nanoribbon's upper boundary is along the $+x$ direction and it is along the $-x$ direction at the lower boundary [see Fig. 8(a1)]. For the right MTI lead, the chiral edge state transmission directions are opposite to that of the left MTI lead.

Next, let us study whether there are the interfacial states along the the domain wall. Consider a perfect MTI nanoribbon with the domain wall at $x = 0$. The nanoribbon is infinite in the y direction with the length L in the x direction, as shown in Fig. 8(b1). Its Hamiltonian is the same as Eq. (2). From its band structure as shown in Fig. 8(b2), we can see that there are four states in the bulk gap. Two of them are the interfacial states and their wave function mainly distribute in the vicinity of the domain wall at $x = 0$, see Fig. 8(b3) [52]. The interfacial states are along the $-y$ direction as shown in Fig. 8(b1).

Based on the above chiral edge states and interfacial states, now we analyze the transport and thermoelectric behaviors of the MTI nanoribbon with a domain wall. When the incident energy E is within the bulk gap, the transport behavior is determined by the chiral edge states. Consider an incident electron from left MTI's lead, this electron propagates along the upper chiral edge state. When it reaches the domain wall, the incident electron is scattered to the two interfacial states $S1$ and $S2$, see Fig. 1(a). Then the electron propagates along the domain wall, until it hits the lower boundary of the nanoribbon and is scattered back along the chiral edge state $R1$ or goes ahead along the chiral edge state $R2$ [52]. The black arrows in Fig. 1(a) show the electron propagation pathway. Figure 9 show the local transport current distribution (the left figure) and local occupation distribution (the right figure), respectively, which clearly exhibit that the incident electron

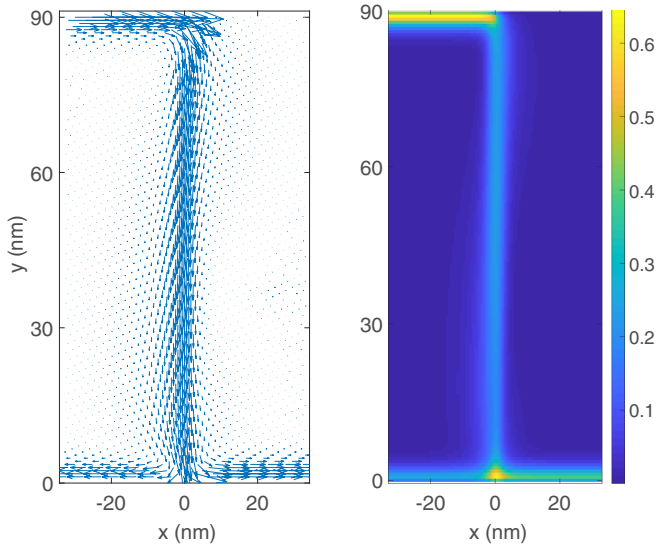

FIG. 9. The left figure shows local transport current distribution J_{ij} and the right figure shows local occupation distribution $n_i^L(E)$ with the incident energy of the electron $E = 0.015$ eV, the azimuthal angle $\phi = 5\pi/12$, the nanoribbon width $W = 90$ nm and the thickness of domain wall $\delta = 1.5$ nm. The other unmentioned parameters are the same as in Fig. 2.

propagates along the pathway mentioned above, i.e., through the chiral edge states and the interfacial states.

When the incident energy E is in the bulk gap ($-\Delta_b < E < \Delta_b$), the transmission coefficient $T(E)$ is determined by the ejection probability from the outgoing edge state $R2$, which depends on the phase difference $\Delta\varphi$ of the two interfacial states $S1$ and $S2$. The phase difference $\Delta\varphi = \Delta kW = (k_{y1} - k_{y2})W$ with the nanoribbon width W and the wave vectors k_{y1} and k_{y2} of the interfacial states $S1$ and $S2$. The wave vector difference $\Delta k = k_{y1} - k_{y2}$ is strongly dependent on the configuration of domain wall and the domain wall thickness δ. For the Bloch wall ($\phi = \pi/2$), the wave vector difference $\Delta k = 0$ [52]. Δk increases with the decrease of ϕ. Δk reaches the maximal value for the Néel wall ($\phi = 0$) [52]. With the increase of the domain wall thickness δ, Δk increases also. So for the incident energy E within the bulk gap, the transmission coefficient $T(E)$ is strongly affected by the nanoribbon width W, the thickness and configuration of the domain walls (see Fig. 2), so are the electric conductance, thermal conductance, Seebeck coefficient, and then the ZT. Therefore, by changing the thickness and configuration of the domain walls and the nanoribbon width W, we can get a large ZT. In addition, for the Bloch wall ($\phi = \pi/2$), the wave vector difference $\Delta k = 0$, so the phase difference $\Delta\varphi$ is independent of the width W, leading to the transmission coefficient and thermoelectric coefficients of the Bloch wall being insensitive to the thickness of the domain wall δ and the nanoribbon width W. On the other hand, when the incident energy E is deep in the conduction band or the valence band (e.g., $E > 2\Delta_b$ or $E < -2\Delta_b$), the bulk states dominate the transport processes, then the transmission coefficient $T(E)$ is always large and is weakly dependent on the configuration and thickness of the domain walls, as shown in Fig. 2. As a result, ZT always is small for $E > 2\Delta_b$ and $E < -2\Delta_b$. Because the transport behavior and the figure of merit ZT in the present device is dominated by the chiral edge states and the interfacial states, and the contribution of bulk states is small. ZT can be regulated by the configuration and thickness of the domain wall, but are independent of the material properties. This is an advantage of the topological system.

IV. THERMOELECTRIC PROPERTIES IN NONLINEAR REGIME

In this section, we explore the thermoelectric properties of the two-terminal MTIs device in the nonlinear regime. Different from the linear case discussed above, there is a temperature gradient $\Delta\mathcal{T}$ and a finite bias between two MTIs leads. The temperature of the right MTIs lead $\mathcal{T}_R$ is the same as the background temperature $\mathcal{T}$ and the temperature of the left MTIs lead is $\mathcal{T}_L = \mathcal{T} + \Delta\mathcal{T}$. The chemical potentials of leads are labeled by μ_L and μ_R ($\mu_R > \mu_L$). In the calculation, we fix μ_L and find the maximum power-generation efficiency η by changing μ_R. The width of the MTIs nanoribbon is set $W = 90$ nm and the thickness of the domain wall $\delta = 1.5$ nm, which are the same as the parameters of linear transport. Figure 10 shows the efficiency η and the equivalent figure of merit ZT_M as functions of the chemical potential μ_L for different temperature gradient $\Delta\mathcal{T}$.

Let us first compare the equivalent figure of merit ZT_M calculated in the nonlinear region with the ZT in the linear response. In Figs. 10(b1) to 10(b3), the thick black lines represent ZT as functions of the Fermi energy E_F in the linear response. We can see from the figure that the ZT of the linear region is completely consistent with the ZT_M (see the red lines in figure) of $\Delta\mathcal{T} = 0.1$ K in the nonlinear region. That is, when the temperature difference $\Delta\mathcal{T}$ tends to 0, the nonlinear ZT_M well returns to the linear ZT, which indicates that our calculations are reasonable and reliable.

At last, we study the thermoelectric properties in the nonlinear regime. As seen in Fig. 10, with the increase of the temperature difference $\Delta\mathcal{T}$ from 0.1 to 100K, the power-generation efficiency η increases regardless of the configurations of domain walls as shown in Figs. 10(a1) to 10(a3), but the equivalent figure of merit ZT_M is not monotonically dependent on $\Delta\mathcal{T}$. For the Néel-type domain wall ($\phi = 0$) and the $\phi = \pi/4$ domain wall, the ZT_M increases first and then slightly decreases with the increase of $\Delta\mathcal{T}$. Here the nonlinear ZT_M can be more than twice the linear ZT [see Figs. 10(b1) and 10(b2)]. For the Bloch-type domain wall ($\phi = \pi/2$), the ZT_M slightly decreases first and then increases again with the increase of $\Delta\mathcal{T}$, see Fig. 10(b3). Moreover, from Figs. 10(a2) and 10(b2) for the configuration of $\phi = \pi/4$ domain wall, the equivalent figure of merit ZT_M can be 1.7 and, in particular, the Carnot power-generation efficiency can reach 26%, when $\Delta\mathcal{T} = 60$ K. Such a large power-generation efficiency η shows a promising application of this thermoelectric device.

V. CONCLUSION

In summary, we study the thermoelectric transport of a two-terminal nanoribbon of the magnetic topological insulator with a domain wall. We explore the role of the domain wall on the thermoelectric properties in the linear and

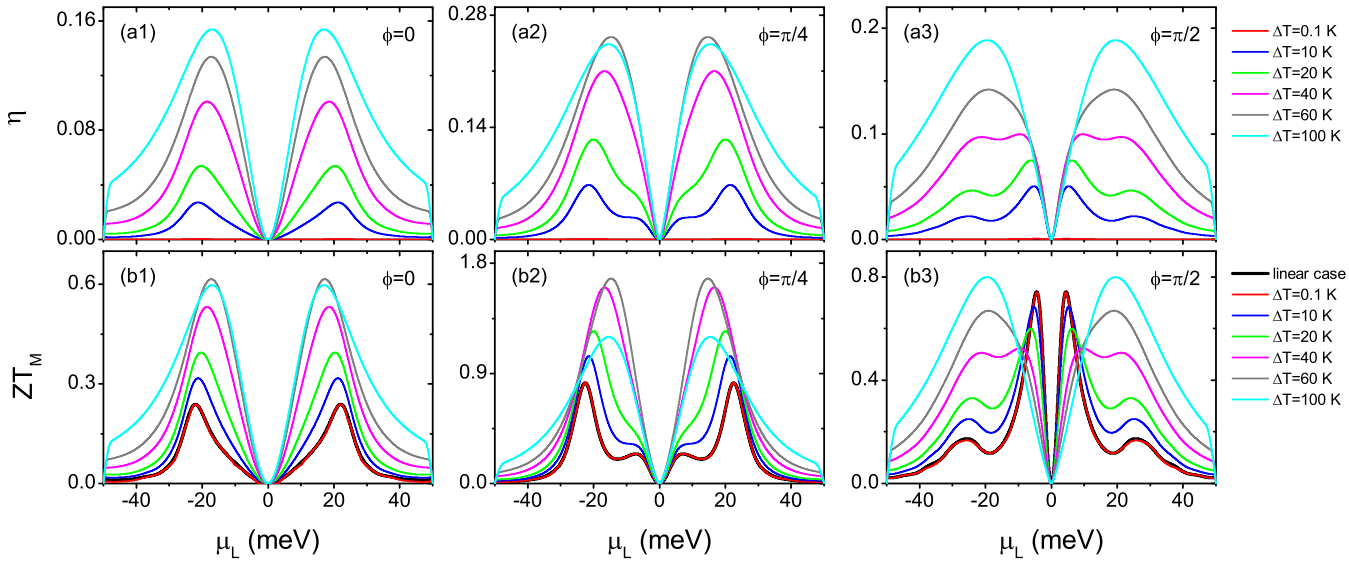

FIG. 10. The efficiency η and the equivalent figure of merit ZT_M as a function of the chemical potential μ_L for different temperature gradient $\Delta\mathcal{T}$, with the background temperature $\mathcal{T}_R = \mathcal{T} = 20$ K, and Néel wall ($\phi = 0$) in (a1), (b1); $\phi = \pi/4$ domain wall in (a2), (b2); and Bloch wall ($\phi = \pi/2$) in (a3), (b3). The thick black lines in (b1), (b2), and (b3) are ZT in the linear regime. The other unmentioned parameters are the same as in Fig. 2.

nonlinear regimes. The Lorenz number L, the Seebeck coefficients S_c, and the thermoelectrical figure of merit ZT are strongly dependent on the configuration of the domain wall, labeled by the azimuth angle ϕ. This means that the thermoelectric properties can be easily adjusted by tuning the configuration of the domain wall. In addition, the thermoelectric coefficients (S_c, ZT) are closely related to the width of the device and the thickness of the domain wall. These results are well illustrated by using the chiral edge states along the nanoribbon boundary and the interfacial states along the domain wall. As to disorder, the transmission coefficient T is robust against strong disorder, and S_c and ZT are robust against moderate disorder. In addition, in the nonlinear case, the high value of the thermoelectric efficiency and the equivalent thermoelectric figure of merit present the potential of this two-terminal setup to achieve high-performance thermoelectricity.

ACKNOWLEDGMENTS

This work was financially supported by the National Key R and D Program of China (Grant No. 2017YFA0303301), NSF-China (Grant No. 11921005), the Strategic Priority Research Program of Chinese Academy of Sciences (Grant No. XDB28000000), and Beijing Municipal Science & Technology Commission (Grant No. Z191100007219013). We acknowledge the High-performance Computing Platform of Peking University for providing computational resources.

[1] H. J. Goldsmid, *Introduction to Thermoelectricity*, Springer Series in Materials Science Vol. 121 (Springer-Verlag, Berlin, 2010).
[2] J. He and T. M. Tritt, Science **357**, eaak9997 (2017).
[3] A. Majumdar, Science **303**, 777 (2004).
[4] M. S. Dresselhaus, G. Chen, M. Y. Tang, R. G. Yang, H. Lee, D. Z. Wang, Z. F. Ren, J.-P. Fleurial, and P. Gogna, Adv. Mater. **19**, 1043 (2007).
[5] K. Saito, G. Benenti, and G. Casati, Chem. Phys. **375**, 508 (2010).
[6] C. Wood, Rep. Prog. Phys. **51**, 459 (1988).
[7] S. Hershfield, K. A. Muttalib, and B. J. Nartowt, Phys. Rev. B **88**, 085426 (2013).
[8] H. Karbaschi, J. Lovén, K. Courteaut, A. Wacker, and M. Leijnse, Phys. Rev. B **94**, 115414 (2016).
[9] G. Gómez-Silva, P. A. Orellana, and E. V. Anda, J. Appl. Phys. **123**, 085706 (2018).
[10] S. Y. Matsushita, K. K. Huynh, H. Yoshino, N. H. Tu, Y. Tanabe, and K. Tanigaki, Phys. Rev. Materials **1**, 054202 (2017).
[11] M. Markov, S. E. Rezaei, S. N. Sadeghi, K. Esfarjani, and M. Zebarjadi, Phys. Rev. Materials **3**, 095401 (2019).
[12] Ł. Karwacki and J. Barnaś, Phys. Rev. B **98**, 075413 (2018).
[13] P. Roura-Bas, L. Arrachea, and E. Fradkin, Phys. Rev. B **97**, 081104(R) (2018).
[14] D. M. T. Kuo, C.-C. Chen, and Y.-C. Chang, Phys. Rev. B **95**, 075432 (2017).
[15] D. Gresta, M. Real, and L. Arrachea, Phys. Rev. Lett. **123**, 186801 (2019).
[16] T. Ming, Y. Wu, C. Peng, and Y. Tao, Energy **80**, 388 (2015).
[17] X. Zhang and L.-D. Zhao, J. Materiomics. **1**, 92 (2015).
[18] G. E. Bulman, E. Siivola, B. Shen, and R. Venkatasubramanian, Appl. Phys. Lett. **89**, 122117 (2006).
[19] L. Müchler, F. Casper, B. Yan, S. Chadov, and C. Felser, Phys. Satus Solidi RRL **7**, 91 (2013).
[20] N. Xu, Y. Xu, and J. Zhu, npj Quantum Mater. **2**, 51 (2017).
[21] J. Liu, Q.-F. Sun, and X. C. Xie, Phys. Rev. B **81**, 245323 (2010).

[22] Y. Xing, Q.-F. Sun, and J. Wang, Phys. Rev. B **80**, 235411 (2009).
[23] M. M. Wei, Y. T. Zhang, A. M. Guo, J. J. Liu, Y. Xing, and Q.-F. Sun, Phys. Rev. B **93**, 245432 (2016).
[24] M. Cutler and N. F. Mott, Phys. Rev. **181**, 1336 (1969).
[25] R. T. Syme and M. J. Kearney, Phys. Rev. B **46**, 7662 (1992).
[26] G. Jeffrey Snyder and E. S. Toberer, Nat. Mater. **7**, 105 (2008).
[27] T. Rejec, A. Ramšak, and J. H. Jefferson, Phys. Rev. B **65**, 235301 (2002).
[28] R. Ma, L. Zhu, L. Sheng, M. Liu, and D. N. Sheng, Phys. Rev. B **84**, 075420 (2011).
[29] S. Onoda, N. Sugimoto, and N. Nagaosa, Phys. Rev. B **77**, 165103 (2008).
[30] R. Venkatasubramanian, E. Siivola, T. Colpitts, and B. O'Quinn, Nature **413**, 597 (2001).
[31] L. D. Hicks and M. S. Dresselhaus, Phys. Rev. B **47**, 16631 (1993).
[32] G. D. Mahan and J. O. Sofo, Proc. Natl. Acad. Sci. USA **93**, 7436 (1996).
[33] A. Shakouri, Annu. Rev. Mater. Res. **41**, 399 (2011).
[34] C. L. Kane and E. J. Mele, Phys. Rev. Lett. **95**, 146802 (2005).
[35] M. Z. Hasan and C. L. Kane, Rev. Mod. Phys. **82**, 3045 (2010).
[36] X.-L. Qi and S.-C. Zhang, Rev. Mod. Phys. **83**, 1057 (2011).
[37] D. Kong, J. C. Randel, H. Peng, J. J. Cha, S. Meister, K. Lai, Y. Chen, Z. X. Shen, H. C. Manoharan, and Y. Cui, Nano Lett. **10**, 329 (2010).
[38] J. Gooth, J. G. Gluschke, R. Zierold, M. Leijnse, H. Linke, and K. Nielsch, Semicond. Sci. Technol. **30**, 015015 (2015).
[39] L.-C. Chen, P.-Q. Chen, W.-J. Li, Q. Zhang, V. V. Struzhkin, A. F. Goncharov, Z. Ren, and X.-J. Chen, Nat. Mater. **18**, 1321 (2019).
[40] X.-L. Qi, Y.-S. Wu, and S.-C. Zhang, Phys. Rev. B **74**, 085308 (2006).
[41] C.-X. Liu, X.-L. Qi, X. Dai, Z. Fang, and S.-C. Zhang, Phys. Rev. Lett. **101**, 146802 (2008).
[42] X.-L. Qi, T. L. Hughes, and S.-C. Zhang, Phys. Rev. B **78**, 195424 (2008).
[43] R. Yu, W. Zhang, H.-J. Zhang, S.-C. Zhang, X. Dai, and Z. Fang, Science **329**, 61 (2010).
[44] K. Nomura and N. Nagaosa, Phys. Rev. Lett. **106**, 166802 (2011).
[45] C.-Z. Chang, J. Zhang, X. Feng, J. Shen, Z. Zhang, M. Guo, K. Li, Y. Ou, P. Wei, L.-L. Wang, Z.-Q. Ji, Y. Feng, S. Ji, X. Chen, J. Jia, X. Dai, Z. Fang, S.-C. Zhang, K. He, Y. Wang, L. Lu, X.-C. Ma, and Q.-K. Xue, Science **340**, 167 (2013).
[46] X. Kou, S.-T. Guo, Y. Fan, L. Pan, M. Lang, Y. Jiang, Q. Shao, T. Nie, K. Murata, J. Tang, Y. Wang, L. He, T.-K. Lee, W.-L. Lee, and K. L. Wang, Phys. Rev. Lett. **113**, 137201 (2014).
[47] K. Yasuda, M. Mogi, R. Yoshimi, A. Tsukazaki, K. S. Takahashi, M. Kawasaki, F. Kagawa, and Y. Tokura, Science **358**, 1311 (2017).
[48] I. T. Rosen, E. J. Fox, X. Kou, L. Pan, K. L. Wang, and D. Goldhaber-Gordon, npj Quantum Mater. **2**, 69 (2017).
[49] Y. Deng, Y. Yu, M. Z. Shi, Z. Guo, Z. Xu, J. Wang, X. H. Chen, and Y. Zhang, Science **367**, 895 (2020).
[50] G. Chen, J. Zhu, A. Quesada, J. Li, A. T. N'Diaye, Y. Huo, T. P. Ma, Y. Chen, H. Y. Kwon, C. Won, Z. Q. Qiu, A. K. Schmid, and Y. Z. Wu, Phys. Rev. Lett. **110**, 177204 (2013).
[51] G. Chen, T. Ma, A. T. N'Diaye, H. Kwon, C. Won, Y. Wu, and A. K. Schmid, Nat. Commun. **4**, 2671 (2013).
[52] Y.-F. Zhou, Z. Hou, and Q.-F. Sun, Phys. Rev. B **98**, 165433 (2018).
[53] Q. Yan, Y.-F. Zhou, and Q.-F. Sun, Chin. Phys. B **29**, 097401 (2020).
[54] M. D. DeJong and K. L. Livesey, Phys. Rev. B **92**, 214420 (2015).
[55] J. Wang, B. Lian, and S. C. Zhang, Phys. Rev. B **89**, 085106 (2014).
[56] R.-X. Zhang, H.-C. Hsu, and C.-X. Liu, Phys. Rev. B **93**, 235315 (2016).
[57] C.-Z. Chen, J. J. He, D.-H. Xu, and K. T. Law, Phys. Rev. B **96**, 041118(R) (2017).
[58] C.-Z. Chen, Y.-M. Xie, J. Liu, P. A. Lee, and K. T. Law, Phys. Rev. B **97**, 104504 (2018).
[59] Y.-H. Li, J. Liu, H. Liu, H. Jiang, Q.-F. Sun, and X. C. Xie, Phys. Rev. B **98**, 045141 (2018).
[60] J. Wang, Phys. Rev. B **94**, 214502 (2016).
[61] T. A. Costi and V. Zlatic, Phys. Rev. B **81**, 235127 (2010).
[62] N.-X. Yang, Y.-F. Zhou, P. Lv, and Q.-F. Sun, Phys. Rev. B **97**, 235435 (2018).
[63] W. Long, Q.-F. Sun, and J. Wang, Phys. Rev. Lett. **101**, 166806 (2008).
[64] N.-X. Yang, Z. Hou, and Q.-F. Sun, Phys. Rev. B **101**, 035418 (2020).
[65] G. Bevilacqua, G. Grosso, G. Menichetti, and G. Pastori Parravicini, Phys. Rev. B **94**, 245419 (2016).
[66] H. Jiang, L. Wang, Q.-F. Sun, and X. C. Xie, Phys. Rev. B **80**, 165316 (2009).
[67] Y. Zhang, J.-P. Hu, B. A. Bernevig, X. R. Wang, X. C. Xie, and W. M. Liu, Phys. Rev. B **78**, 155413 (2008).
[68] S. Nakanishi and M. Tsukada, Phys. Rev. Lett. **87**, 126801 (2001).
[69] A.-P. Jauho, N. S. Wingreen, and Y. Meir, Phys. Rev. B **50**, 5528 (1994).
[70] V. Zlatić and J. K. Freericks, Phys. Rev. Lett. **109**, 266601 (2012).
[71] K. B. Masood, P. Kumar, R. A. Singh, and J. Singh, J. Phys. Commun. **2**, 062001 (2018).
[72] G. Ding, G. Gao, and K. Yao, Sci. Rep. **5**, 9567 (2015).
[73] T. Gunst, T. Markussen, A.-P. Jauho, and M. Brandbyge, Phys. Rev. B **84**, 155449 (2011).
[74] W. Mao and K. S. Bedell, Phys. Rev. B **59**, R15590(R) (1999).